



Simple and green synthesis of calcium alginate/AgCl nanocomposites with low-smoke flame-retardant and antimicrobial properties

Xin Zhang · Qing Zhang · Yun Xue · Yanwei Wang · Xiaodong Zhou · Zichao Li · Qun Li

Received: 5 November 2020 / Accepted: 9 March 2021 / Published online: 22 March 2021
© The Author(s), under exclusive licence to Springer Nature B.V. 2021

Abstract Fire hazards and infectious diseases result in great threats to public safety and human health, thus developing multi-functional materials to deal with these issues is critical and yet has remained challenging to date. In this work, we report a facile and eco-friendly synthetic approach for the preparation of calcium alginate/silver chloride (CA/AgCl) nanocomposites with dual functions of excellent flame-retardant and antibacterial activity. Multi characterization techniques and antibacterial assays were performed to investigate the flame-retardant and antibacterial properties of the CA/AgCl nanocomposites. The obtained results show that the CA/AgCl nanocomposites exhibited much higher limiting oxygen index value ($> 60\%$) than that of CA (48%) with a UL-94 rating of V-0. Moreover, CA/AgCl particularly displayed an efficiently smoke-suppressive feature by achieving a total smoke release value of $2.7 \text{ m}^2/\text{m}^2$, which was reduced by 91%, compared to CA. The antibacterial

rates of the CA/AgCl nanocomposites against *E. coli* and *S. aureus* were measured to be 99.67% and 99.77%, respectively, while CA showed quite weak antibacterial rates. In addition, the flame-retardant and antibacterial mechanisms were analyzed and proposed based on the experimental data. This study provides a novel nanocomposite material with both flame-retardant and antibacterial properties which show promising application prospects in the fields of decorative materials and textile industry.

Keywords Alginate polysaccharides · AgCl · Flame-retardant · Pyrolysis · Antibacterial mechanism

Introduction

Fire is one of the most permanent and serious disasters that endangers human society. The smoke from fire can hinder the extinguishing of fire and affect the escape of people, which has been the main cause of the suffocation and casualties. Hence, it has always been critical to design materials with reliable flame-retardant and smoke emission-suppressive properties. Meanwhile, it also arouses major concern as public places are usually the main transmission medium for many infectious diseases including hepatitis, influenza, dysentery, trachoma, tinea pedis, novel coronavirus pneumonia and others [1]. Therefore, it is

X. Zhang · Q. Zhang · Y. Xue · Y. Wang · X. Zhou · Q. Li (✉)

College of Chemistry and Chemical Engineering, Shandong Collaborative Innovation Center of Marine Biobased Fibers and Ecological Textiles, Qingdao University, Qingdao 266071, China
e-mail: qunli@qdu.edu.cn

Z. Li (✉)

Institute of Biomedical Engineering, College of Life Sciences, State Key Laboratory of Bio-Fibers and Eco-Textiles, Qingdao University, Qingdao 266071, China
e-mail: zichao.li@qdu.edu.cn

desirable to achieve high-performance flame-retardant materials with antibacterial function when applied in public places such as the transportation, theaters, shopping mall, in order to overcome the problem of the harm of fires and infectious diseases simultaneously.

Alginate, constituted of β -D-mannuronic acid (M block) and α -L-guluronic acid (G block), is a polysaccharide with abundant natural reserves (Das et al. 2017; Liu et al. 2016c; Luo et al. 2015). As a renewable biomass, it is preferable for its intrinsic features including non-toxic, well degradability and biocompatibility (Das et al. 2017; Googerdchian et al. 2012; Lee and Mooney 2012), and thus it has attracted great interest in recent years (Li et al. 2017a, b; Liu et al. 2015a; Senturk Parreidt et al. 2018). Based on these reports, calcium alginate (CA) has been proved to be a desirable material for applications in the textile industry (Agnieszka Kyzioł; Mokhena and Luyt 2017a) due to its inert nature and good flame retardant property, although its mechanism still needs to be clarified (Shao et al. 2019; Wang et al. 2015). Noticeably, the studies have shown that the limiting oxygen index (LOI) value of CA was around 34, which is limited as a desirable flame-retardant agent. Moreover, CA itself has not been verified as a multi-functional material, for instance, it exhibited almost no antibacterial activity. In this aspect, it is essential to improve the flame retardancy of CA for practical application, and meanwhile to gain more functions to broaden its utilization.

Composite materials enable various components to complement each other in performance and produce the synergistic effects through the interaction of two phases, so that the comprehensive performance of composite materials could be better than that of the original constituent materials to meet different demands (Lee et al. 2015; Li et al. 2015). Our previous studies indicate that alginate is a suitable biological matrix to synthesize functional nanocomposites with the advantages of both resource conservation and environmental protection (Liu et al. 2018b; Xu et al. 2019). The alginate grid not only displayed the ability to guide the growth of inorganic nanoparticles (NPs), but also prevented the formed NPs from aggregation and acted as a stabilizer as well (Kou and Varma 2012). Moreover, in terms of native alginate, the synthesis of alginate-NP based composites has been proved to be an efficient approach to improve the

flame retardancy (Liu et al. 2018a; Xu et al. 2019). For instance, zinc alginate/nano-Cu₂O composites exhibited enhanced thermal stability and flame-retardant properties with a limiting oxygen index of 58 compared to zinc alginate. The combustion behavior of the formed CA/calcium borate composites showed excellent anti-dripping properties, while thermogravimetric analysis (TGA) indicated that the formed composites could validly inhibit the heat transmission with more char residue. Nonetheless, the amount of smoke emission for the alginate-based composites was comparatively high based on our previous works. Furthermore, the alginate materials commonly tend to have single function, which cannot fulfill multiple demands and are restrained in practical use (Liu et al. 2018a, 2018b; Xu et al. 2019). Therefore, it is of great significance to synthesize smoke-suppressive flame retardants with multi-functions that are derived from the natural resource of alginate, although it is generally being challenging.

Herein, we report the in-situ synthesis of nano-silver chloride (nano-AgCl) in the alginate polysaccharide matrix to obtain the CA/AgCl nanocomposites by achieving enhanced flame retardancy and excellent antibacterial properties. The characterization techniques including X-ray diffractometry (XRD), Fourier transform infrared spectroscopy (FT-IR), transmission electron microscopy mapping (TEM-mapping), and TGA was employed to investigate the basic properties of the CA/AgCl nanocomposites. The combustion behavior was studied by limiting oxygen index (LOI), vertical burning tests (UL-94), and cone calorimetry (CONE). Moreover, its antibacterial activity was evaluated by the disc diffusion and colony-forming unit (CFU) assay. Furthermore, thermogravimetric analyzer coupled with Fourier transform infrared analysis (TG-FTIR) and pyrolysis–gas chromatography-mass spectrometry (Py-GC-MS) were performed to explore the thermal degradation mechanism, while the fluorescence detection of the reactive oxygen species (ROS) and the images of bacterial morphology change was carried out to illustrate the antibacterial mechanism of materials. Our study presents a facile preparation strategy for alginate-based nanomaterials with dual functions of flame-retardant and antibacterial properties, and also provides deep insights into their functional mechanisms.

Experimental

Reagents

Sodium alginate (Viscosity range 105–115 mPa·s, $G/M = 1.83$, $M_W = 447,823$, $M_N = 375,577$) was obtained from Guangfu Fine Chemical Research Institute (Tianjin, China). Silver nitrate, calcium chloride anhydrous and ammonia solution were purchased from Sinopharm Chemical Regent Co., Ltd (Shanghai, China). All the chemicals were of analytical grade and applied without further purification.

Preparation of CA.

In brief, 3 g of sodium alginate was added to 100 mL deionized water at 50 °C for 2 h with constant stirring to form a homogenous sol, which was shaped by a certain mold and immersed in 1 L of 4% calcium chloride solution for 4 h. Finally, the crosslinked gel was washed with distilled water for three times and dried to obtain CA.

Preparation of CA/AgCl nanocomposites

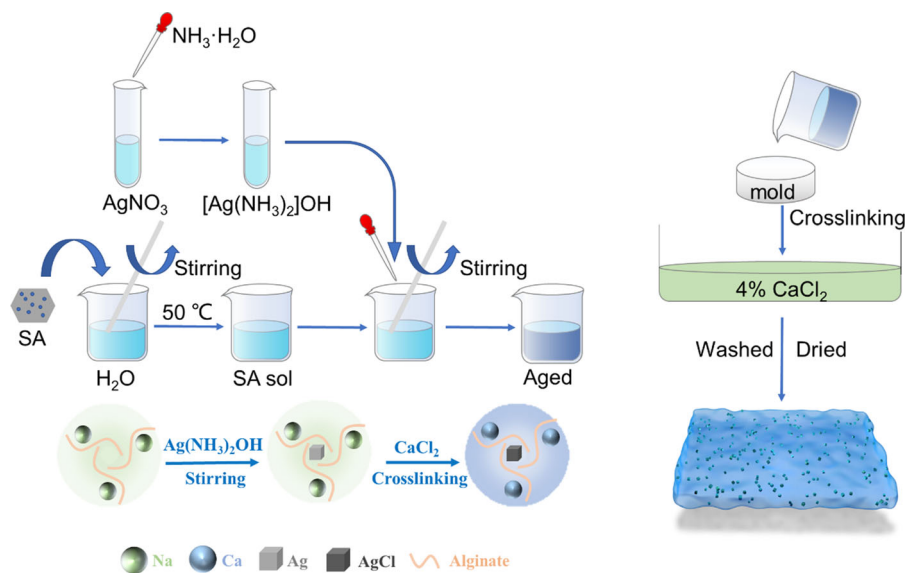
The CA/AgCl was prepared through a simple and green method as illustrated in Scheme 1. Briefly, 3 g of sodium alginate was dissolved in 100 mL deionized water at 50 °C for 2 h with constant stirring to form a homogenous sol. Subsequently, 0.3 g $AgNO_3$ was dissolved in 10 mL H_2O , and the ammonia solution

was added dropwise until the solution became clear. Then the freshly prepared silver ammonia solution (0.3 g $AgNO_3$, 5 mL H_2O , 0.45 mL ammonia solution, 25 °C) was added dropwise under constant stirring for 5 min and aged for 30 min. The sol was poured into the mold, and then immersed in the calcium chloride solution (30 g/L, 25 °C, 4 h) for crosslinking. Finally, the obtained transparent hydrogel was washed with distilled water and dried with freezer dryer (FD-1A-50, Billing Instrument Manufacturing, China) to obtain the CA/AgCl nanocomposites.

As shown in Scheme 1, during the calcification process, both calcium and sodium ions were replaced in situ, the structure of the alginic acid macromolecular chain remained unchanged, and the functional groups on the M-block and G-block formed intermolecular hydrogen bonds with the cross-linked AgCl. Therefore, the spatial structure of the formed CA/AgCl nanocomposites became more durable.

Characterizations

The XRD (D8 ADVANCE, Bruker, Germany) was occupied to analyze the components of the nanocomposites with Ni-filtered $Cu-K\alpha$ radiation ($\lambda = 0.154$ nm) in the range of 5°–80° (2θ). FT-IR (NICOLET iS50, Thermo Fisher Scientific, USA) was employed to detect changes among functional groups



Scheme 1 Schematic illustration for the preparation of CA/AgCl nanocomposites

in the matrix of alginate biopolymer. The representative elements and distribution of CA/AgCl were exhibited by TEM-mapping (Tecnai G2 F20, FEI, USA). The morphologies of the CA and CA/AgCl were observed by TEM (XMAX 80 T, Oxford, USA). TGA was performed on a thermal analyzer (SDT Q600, TA Instruments, USA) under both air and nitrogen atmosphere, while the sample was heated from room temperature to 800 °C at a heating rate of 10 °C/min in nitrogen atmosphere.

Flame retardant performances

LOI and UL-94 tests

The LOI tests were performed on a digital limiting oxygen index tester (LFY-606B, Shandong Textile Science Research Institute, China) according to ISO 4589-1:1996. The UL-94 tests were performed on a burning rate tester (LFY-601A, Shandong Textile Science Research Institute, China) according to ANST/UL-94–1985.

CONE

The combustion behavior was examined by a cone calorimeter (FTT0242, Fire Testing Technology, UK) under an external heat flux of 50 kW/m², according to ISO 5660. The dimensions of all samples were 100 mm × 100 mm × 2 mm.

TG-FTIR

TG-FTIR measurements were conducted by a TG analyzer (STA6000, PerkinElmer instruments, USA) coupled with a FTIR spectrometer (Perkin-Elmer Frontier, USA). The sample was heated from 30 to 700 °C in nitrogen atmosphere with a gas flow rate of 50 mL/min and the heating rate of 20 °C/min.

Py-GC-MS

Py-GC-MS was tested via a pyrolysis analyzer (EGA/PY-3030D, Frontier, Japan) coupled with a gas chromatograph (Trace 1310, Thermo Scientific, USA). The composites were processed under a heating rate of 20 °C/min in helium atmosphere, and then the products were compared with the National Institute of

Standards and Technology (NIST) library and others standard database library.

Antibacterial tests

The disc diffusion and colony-forming assays were performed to examine the antibacterial activities of CA and CA/AgCl. *E. coli* (ATCC 25922) was cultivated in lysogenic broth medium and *S. aureus* (ATCC 6538) was grown in 7.5% of sodium chloride broth medium at 37 °C overnight, respectively.

Disc diffusion assay

The tests for the inhibition zone were based on AATCC-90 (Halo Test) (Zhang et al. 2018a). The sterilized plate agar was poured into petri dishes and cooled. Subsequently, 50 µL suspension of *E. coli* and *S. aureus* was spread on the agar surface evenly. Then the hydrogel was subjected to the plate agar surface and incubated at 37 °C in darkness for 24 h. The effect of the inhibition zone can be judged by preliminary observation. The antibacterial activity of the samples was evaluated by a method reported in the literature, in which the antibacterial action was rated “good” (zone of inhibition > 1 mm), “fairly good” (zone of inhibition ≤ 1 mm), “sufficient” (growth up to, but not on the hydrogel), “limited” (limited growth on the hydrogel) or “poor” (hydrogel is overgrown with bacteria ≥ 50%) (Pollini et al. 2009). The zone of inhibition was expressed as the diameter of no bacterial growth minus the diameter of the hydrogel. The inhibition zone can directly show the antibacterial properties of the nanocomposites.

Colony-forming unit assay

CA/AgCl was dissolved in phosphate buffer saline (PBS) to obtain a 10 mg/L of solution. The bacterial suspension was diluted to 10²–10³ CFU mL⁻¹, and 50 µL mixed solution was pipetted to mix with the dissolved one. After incubation, the mixed solution was pipetted to be cultivated at 37 °C overnight. Finally, the number of colonies was counted and the percentage of inhibition rate was expressed as the following Eq. (1) (Sedighi and Montazer 2016):

Antibacterial percentage = (control group-experimental group)/control group × 100%

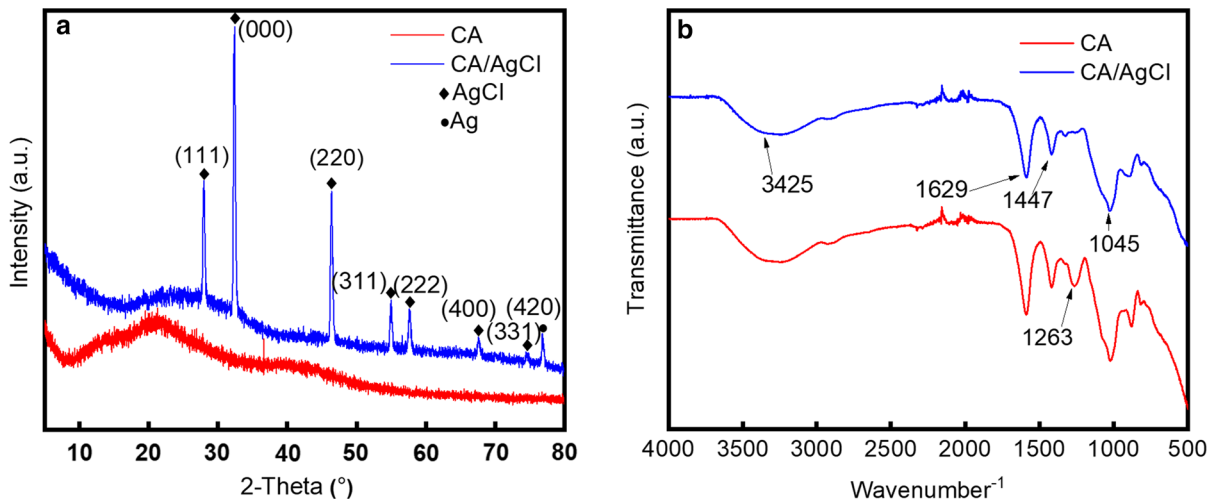


Fig. 1 XRD patterns (a) and FT-IR spectra (b) of CA and CA/AgCl

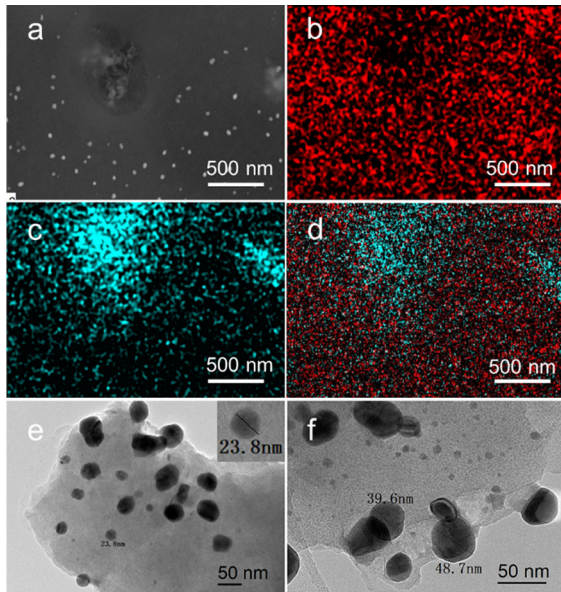


Fig. 2 Selective area TEM image of CA/AgCl (a); elemental mapping images of Ca (b), Ag (c), elements superimposed images (d); and TEM images of the typical CA/AgCl nanocomposites (e, f)

All the materials were sterilized in an autoclave before tests. Each sample was performed in triplicate and the results were expressed as the mean (Gao et al. 2019).

Microstructural changes of the bacteria

Bio-scanning electron microscope (bio-SEM) (SU8010, Hitachi, Japan) was generally applied to observe the deformation and damage of the outer surface of cells, which also showed the distribution of the antibacterial agents on the cell surface. The bacterial suspension was treated with CA/AgCl and washed with PBS (pH = 7.4) after centrifugation at 3000 r/min for 10 min. The concentrated bacterial colonies were collected and fixed with 2.5% glutaraldehyde at 4 °C for overnight. Bacterial cells were dehydrated with graded ethanol. The sample was placed on the conductive glue and dried for observation. For comparison, the untreated bacteria were selected as the control group.

Detection of reactive oxygen species (ROS)

The release level of ROS was detected by the fluorescence label 2',7'-dichlorodihydrofluorescein diacetate (DCFH-DA) (CAS: 4091-99-0). Briefly, the bacteria were treated with DCFH-DA in dark for 30 min. The experimental groups were treated with CA/AgCl for 15 and 30 min, respectively. Then the samples were rinsed with PBS for several times. Finally, the generation of ROS and the fluorescent images were analyzed with a confocal microscope (FV1200, Olympus, Japan).

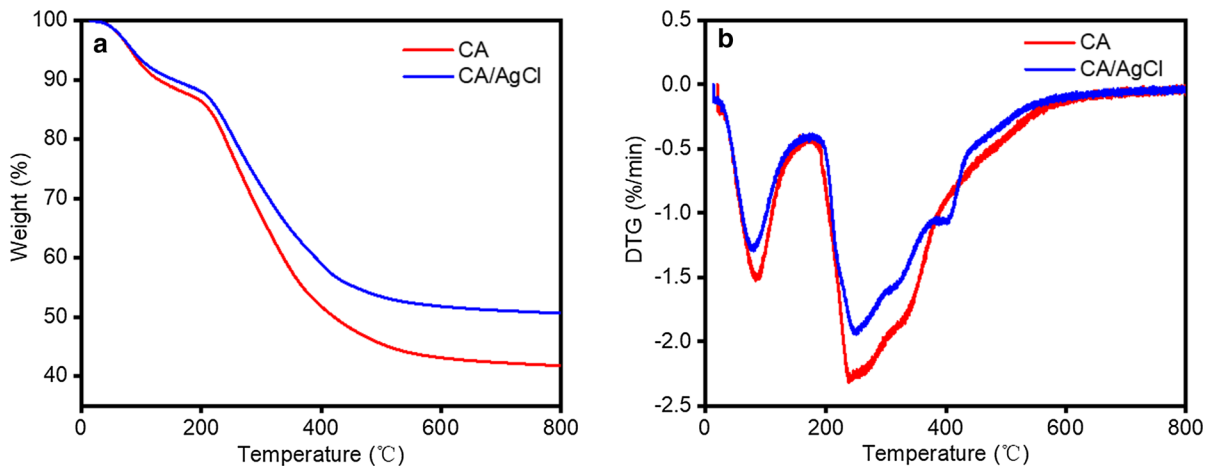


Fig. 3 TGA (a) and DTG (b) curves of CA and CA/AgCl under N_2

Table 1 Main data of TG and DTG analysis

Samples	$T_{5\%}$ (°C)	$T_{10\%}$ (°C)	T_{max1} (°C)	T_{max2} (°C)	Residue at 700 °C (%)
CA	83 ± 2	129 ± 3	82 ± 4	238 ± 2	42.9 ± 0.3
CA/AgCl	85 ± 3	154 ± 1	87 ± 2	257 ± 1	51.7 ± 0.5

Table 2 LOI, UL-94 and combustion parameters of CA and CA/AgCl

Sample	LOI (%)	UL-94	THR (MJ/m ²)	PHRR (kW/m ²)	TSR (m ² /m ²)	Residue (%)
CA	48 ± 1	V-0	2.5 ± 0.1	53 ± 4	30.0 ± 1.2	33.1 ± 0.8
CA/AgCl	> 60	V-0	2.4 ± 0.1	12 ± 1	2.7 ± 0.5	47.4 ± 0.3

*LOI, limiting oxygen index; UL-94, vertical burning test; THR, total heat release; PHRR, peak heat release rate; TSR, total smoke release

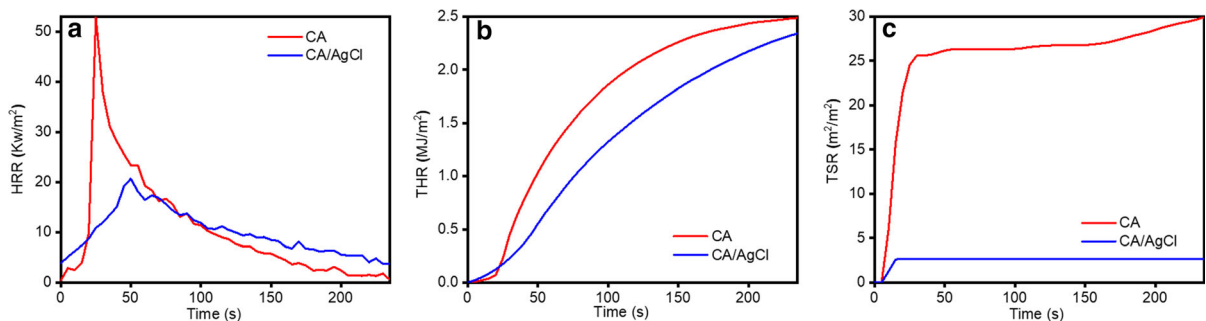


Fig. 4 HRR, THR and TSR curves of CA and CA/AgCl trend with time

Statistical analysis

Results were expressed as a mean value with standard deviation (mean \pm S.D.) of each sample that is repeated three times and the results were expressed as the mean.

Results and discussion

Characterizations of CA/AgCl

The XRD patterns of CA and CA/AgCl are shown in Fig. 1a. The peaks at $2\theta = 27.8^\circ$ (111), 32.2° (000), 46.3° (220), 54.8° (311), 57.6° (222), 67.4° (400), 74.5° (331), and 76.6° (420) are attributed to the typical cubic phase of metallic AgCl (JCPDS file:31-1238), which identify the formation of AgCl crystals (Zhang et al. 2018a). The FT-IR absorption peaks of CA and CA/AgCl are displayed in Fig. 1b, in which the broad peaks at 3425 cm^{-1} are ascribed to the stretching vibration of the $-\text{OH}$ bond. The peak at 1629 cm^{-1} corresponds to the vibration of the $-\text{COO}$ bond (Zhao et al. 2018), and the peak at 1447 cm^{-1} is attributed to the $-\text{CH}_2$ bond, while the peak at 1045 cm^{-1} is assigned to the $\text{C}-\text{O}-\text{C}$ bond (Luo et al. 2015). In addition, it can be observed that the absorption peaks of the nanocomposites at 1629, 1263 and 1045 cm^{-1} are weakened, which may be related to the change of the force field around the hydrogen atoms after the formation of hydrogen bonds, while the absorption peaks shift to low frequencies. The absorption peaks at 1263 and 1447 cm^{-1} can be assigned to the stretching vibration of the $\text{C}-\text{O}$ bond. All the above-presented results indicate the successful synthesis of CA/AgCl nanocomposites.

TEM was performed to explore the distribution of AgCl NPs in CA matrix and the results are shown in Fig. 2. It can be seen from Fig. 2a that AgCl NPs are dispersed in the continuous phase of CA. Figure 2b, c reveal the distribution of calcium and silver elements, respectively. The superimposed images of calcium and silver element are displayed in Fig. 2d. It can be observed that they are hybridized with each other, and the distribution is relatively uniform. As seen in Fig. 2e, f, the morphology of nano-AgCl is mono-dispersed with a size from 20 to 50 nm, suggesting that the simple green in-situ synthetic process successfully avoid the agglomeration of nano-AgCl. We suggest that the positioning effect of carboxyl groups on anions as well as the entanglement and stabilization effects of macromolecular chains on NPs contribute to the formation of non-agglomerated nano-AgCl.

The thermal stability of both CA and CA/AgCl under nitrogen atmosphere was investigated by TG-DSC and the curves are plotted in Fig. 3 with the main data listed in Table 1. It can be found that both samples display similar reaction trends. The original weight losses ($T_{5\%}$) of CA and CA/AgCl appeared at 83 and 85°C , respectively. In the initial stage, the temperature of maximum rate ($T_{\text{max}1}$) was 82 and 87°C , which are ascribed to the loss of crystal water and free water. However, in the second stage, their rates of weightlessness were accelerated in two independent decomposition steps at $90\text{--}647^\circ\text{C}$ and $87\text{--}701^\circ\text{C}$, respectively, which can be ascribed to the decomposition of alginate. As a typical organic substance, CA shows weight loss $T_{\text{max}2}$ at 238°C , while obtaining char residue about 42.9%. As for CA/AgCl, the second stage has a higher char residue of about 51.7% at $T_{\text{max}2}$ of 257°C . Furthermore, the char residue increased by 8.8%, which can be assigned to the catalysis of AgCl

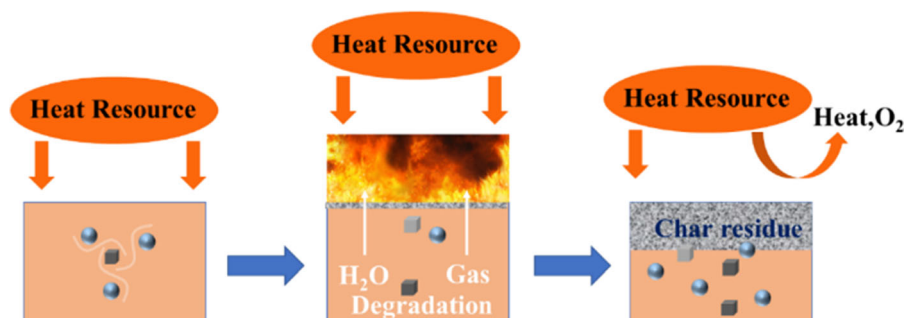


Fig. 5 Schematic diagram of char residue layer formation

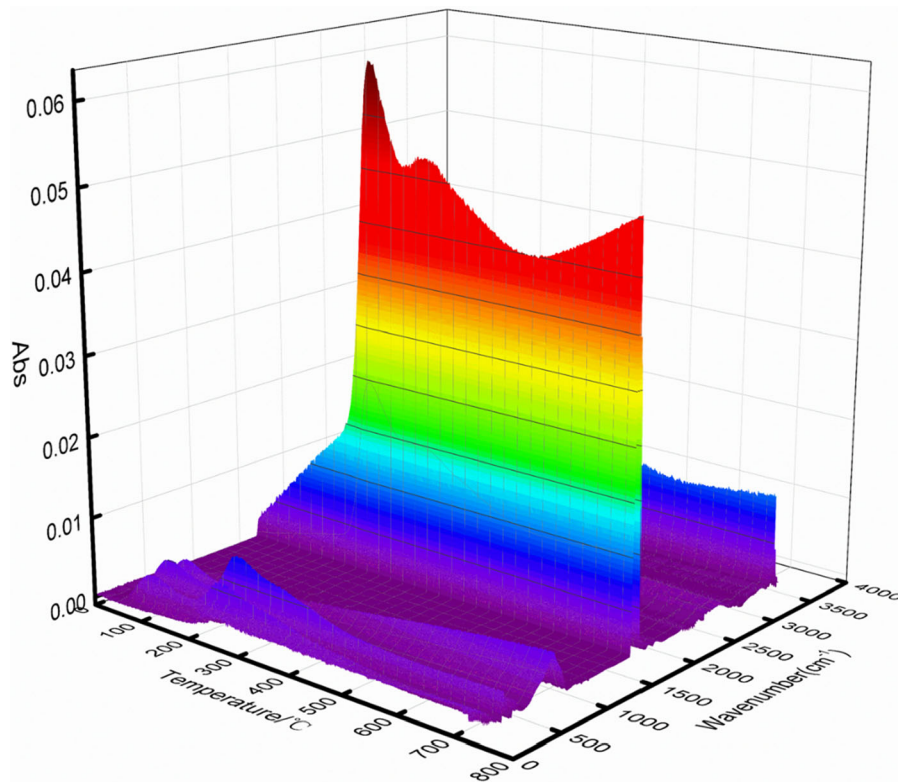


Fig. 6 3D image of CA/AgCl nanocomposites obtained from TG-FTIR

for promoting the formation of char residue. The presence of AgCl reduces the thermal decomposition rate of the nanocomposites and catalyze organic matter to form a char residue layer, thus improving their flame-retardant properties. The increase of the char residue ratio indicates that the combustion part was reduced and the flame-retardant property for the nanocomposites was improved.

Flame-retardant performance

LOI, UL-94 and CONE tests

The flame-retardant property was studied by the LOI and UL-94 tests and the data are displayed in Table 2. Samples were extinguished in 10 s and maintained their initial shape without dripping, which are classified as V-0. Furthermore, for comparison the LOI value is increased from 48 (CA) to 60 (CA/AgCl), confirming that the introduction of AgCl markedly enhanced the flame retardancy of CA.

CONE is currently the most ideal test instrument that can characterize the combustion performance of composites. Its test environment is close to the real combustion environment of the fireproof materials, and the obtained test data can evaluate the combustion behavior of composites in fires (Ma et al. 2017). The heat release rate (HRR), total heat release (THR) and total smoke release (TSR) are the important parameters to characterize the fire safety and the spread of fire (Nabipour et al. 2020; Wang et al. 2018). The combustion behavior related data are listed in Table 2 and the curves are depicted in Fig. 4. The peak of the heat release rate (PHRR) and TSR of CA/AgCl is much lower than of CA, indicating the better flame-retardant performance of the nanocomposites. Meanwhile, the THR of both CA and CA/AgCl are at a low level. In addition, the residue of CA/AgCl (47.4%) is higher than that of CA (33.1%), which corresponded to the data of weight loss in TGA.

AgCl NPs could catalyze organic matter to form a char residue, which blocked the air and prevented further combustion of the nanocomposites (Mu et al.

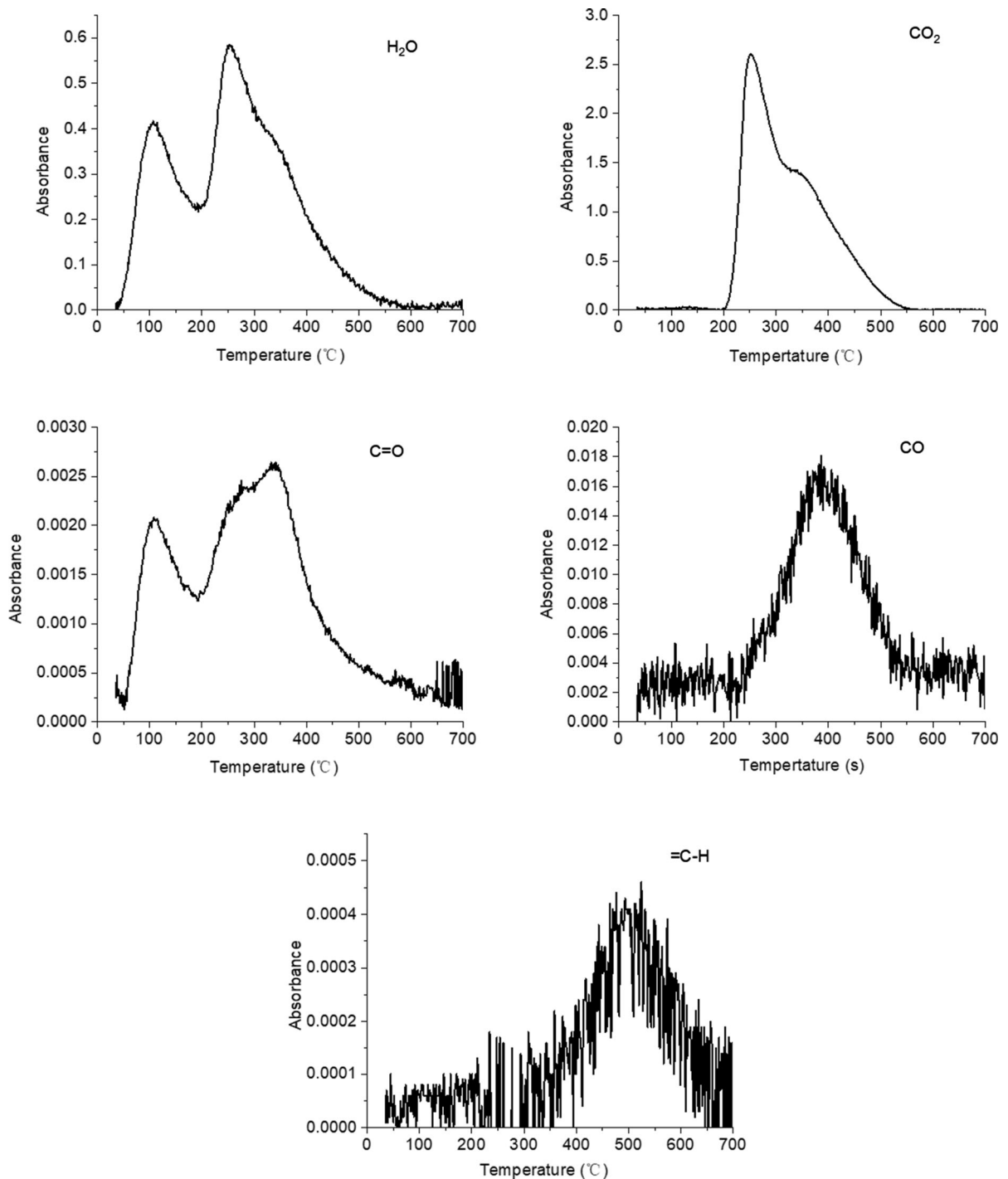


Fig. 7 FT-IR spectra of typical groups as a function of temperature for CA/AgCl

2017), resulting in a decrease in smoke and heat release (Wang et al. 2016). The formation process of char residue is shown in Fig. 5. In a fire, the smoke is

an important cause of casualties, thus low smoke emission is of great importance for protecting human lives. Since the amount of smoke released from CA/

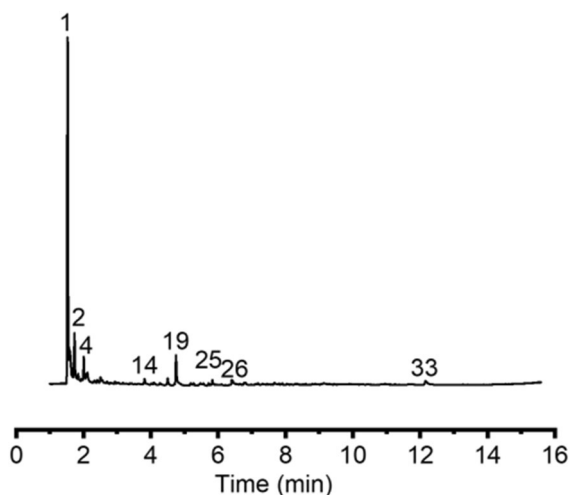


Fig. 8 PY–GC–MS detection of gas products evolved from pyrolysis of CA/AgCl

AgCl is 91% lower than that of CA, we suggest that CA/AgCl is an excellent low-smoke composite. The aforementioned results indicate that CA/AgCl possess much better flame-retardant property than that of CA.

TG-FTIR

TG-FTIR was employed to study the thermal degradation performance of CA/AgCl nanocomposites. Figure 6 shows the 3D FTIR spectrum of the gas generated during the thermal degradation of CA/AgCl nanocomposites, in which the information of wavenumber, infrared absorbance and time are included.

It can be observed from Fig. 6 that most of the pyrolysis process took place in the temperature range of 228–700 °C, and the main products are CO₂ (2364–667 cm⁻¹) and H₂O (3730–3500 cm⁻¹) (Wang et al. 2018). In order to further understand the changing trends for the absorbance of various functional groups towards temperature, the infrared spectra of several functional groups were selected for preliminary analysis, as shown in Fig. 7. It can be found that the primary gaseous products are H₂O and CO₂, flammable components released = CH, –C = O, CO groups and wave numbers of the functional group were as following: H₂O, 3730 cm⁻¹; = CH, 3016 cm⁻¹; CO₂, 2364 cm⁻¹; CO, 2180 cm⁻¹; C = O, 1752 cm⁻¹ (Liu et al. 2015b). The changes of the absorbance of the above functional groups with

temperature are shown in Fig. 7. It is clear that H₂O and –C = O are mainly produced in the first and second pyrolysis stages of CA/AgCl, while CO₂ is mainly generated in the second stage of pyrolysis. Meanwhile, the compounds containing = CH groups mainly appears in the high temperature area (Liu et al. 2016b).

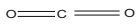

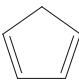
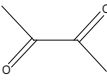
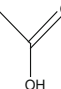
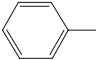
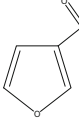
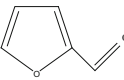
It can be known from Fig. 7 that the H₂O and –C = O groups are produced in the primal pyrolysis stage (low-temperature area), and the = CH fragments are generated in the third pyrolysis stage (high-temperature area) (Zhang et al. 2018b). The absorbance of above functional groups varied with temperature. H₂O and CO₂ are generated at the low temperature and H₂O is generated a little earlier than CO₂, which can be ascribed to the release of crystal water in the nanocomposites. However, the absorbance intensity of CO₂ is much higher than that of H₂O, which can be attributed to the catalysis of silver, making thermal degradation preferred to decarboxylation. The = CH groups are mainly yielded at the high-temperature area, indicating that these compounds have a further degradation stage at the high temperature to release = CH. In addition, CO occurred in the second pyrolysis stage, and the intensity stays at a high level at the high temperature, suggesting further pyrolysis process can generate CO.

The aforementioned results briefly explain the pyrolysis process, including dehydration, decarboxylation and cleavage. Fractures of glycosidic bonds were emerged at the second pyrolysis stage, with the production of CO₂, H₂O, –C = O and char residues. The fragments were pyrolyzed into more stable char residue and released CO and = CH groups, when the temperature rose (Zhang et al. 2016).

PY–GC–MS

The PY–GC–MS analysis was carried out to investigate the pyrolytic gaseous components of CA/AgCl. Comparing with the NIST library, the highest possibility of gaseous compounds identification was acquired (Liu et al. 2016b). The ion intensities of gaseous products are shown in Fig. 8. The peaks of all the products were marked with labels, which corresponded to the numbers in Table S1 and the main products are listed in Table 3. According to the information in Fig. 8 and Table 3, the major pyrolysis products are identified to be CO₂, acetone, 2,

Table 3 Analytical results of chemical constituents of 700 pyrolysis products of CA/AgCl

Label	T _R (min)	Molecular formula	Name of compound	Molecular structure	Mw (g/mol)	Peak area (%)
1	1.53	CO ₂	Carbon dioxide		44	57.43
2	1.73	C ₃ H ₆ O	Acetone		58	7.06
3	1.84	C ₅ H ₆	1,3-Cyclopentadiene		66	0.77
4	2.01	C ₄ H ₆ O ₂	2,3-Butanedione		86	2.95
5	2.11	C ₂ H ₄ O ₂	Acetic acid		60	2.33
6	3.81	C ₇ H ₈	Toluene		92	1.21
7	4.50	C ₅ H ₄ O ₂	3-Furaldehyde		96	1.39
8	4.75	C ₅ H ₄ O ₂	Furfural		96	5.61

3-Butanedione, acetic acid, toluene and furfural with the total yields of 78.75%. the dehydration, decarboxylation, disproportionation and ring-opening were related reactions during the pyrolysis process (Liu et al. 2015c). The pyrolysis mechanism of CA/AgCl was proposed, as shown in Fig. 9. Alginate molecule was broken into M and G blocks, while the decarboxylation and esterification occurred. However, the yield of CO₂ is much higher than other components with the catalysis of Ag⁺, indicating that the proportion of decarboxylation is higher than that of the dehydration reaction. The fracture of the glycosidic bonds led to many intermediate reactions (Liu et al. 2016a), in which the intermediate compounds are produced by the dehydration, rearrangement, and decarboxylation reactions to obtain small molecules, producing a large amount of CO₂, H₂O, and other

lower heat value compounds to improve the flame retardancy of CA/AgCl.

The main absorption peaks were almost the same, compared to the TG-IR results of CA (Fig. S1 and S2). The absorbance peak of H₂O is much stronger than CA, and more CO₂ was released above 500 °C. In addition, the absorbance of C = O, CO and = C-H are much weaker, indicating that less flammable components were released from CA/AgCl. Hence, the formed CA/AgCl nanocomposites exhibit more excellent flame-retardant property.

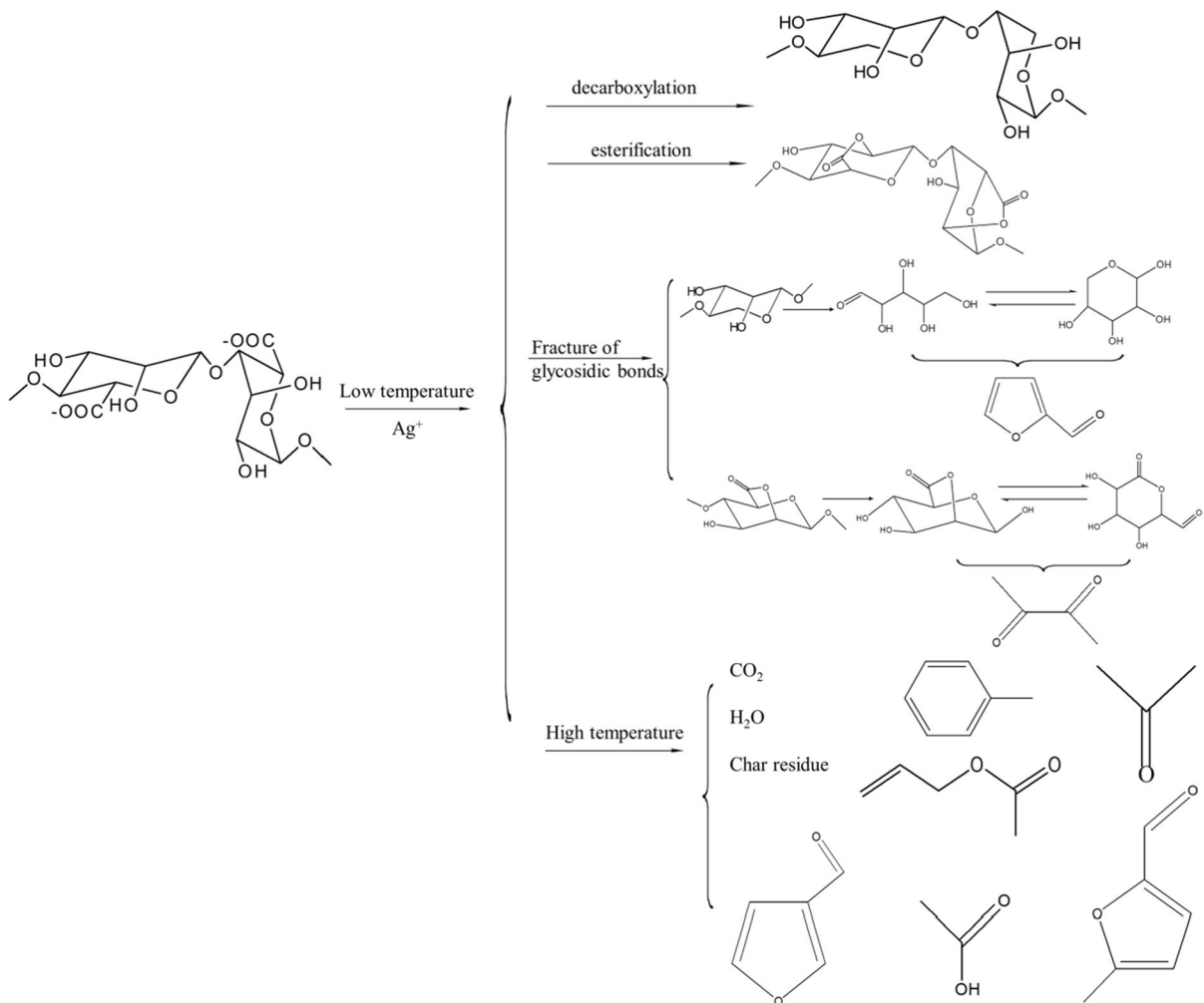


Fig. 9 Speculative pyrolysis mechanism of CA/AgCl

Antibacterial property

Antibacterial performance and rate

The results for the zone of inhibition are shown in Fig. 10. It can be found that CA showed no antibacterial or quite weak antibacterial properties for both *E. coli* and *S. aureus*. As seen in Fig. 10a, c, there was no inhibition zone formed around the hydrogels because alginate did not contain antibacterial functional groups. After the combination with AgCl, silver ions played a major antibacterial role in the nanocomposites (De Silva et al. 2018). The width of inhibition area against both of the bacterial strains was larger than 1 mm, as shown in Fig. 10b, d, which exhibited enhanced antibacterial capability. The results of the

colony CFU confirmed the data from the agar diffusion experiments.

The control groups of *E. coli* and *S. aureus* colonies were cultivated to 10^2 – 10^3 CFU cm^{-1} for calculating the antibacterial rates. Both CA and CA/AgCl were mixed with bacteria. The colonies were counted and the data are listed in Fig. 10e. Notably, the antibacterial rates of *S. aureus* and *E. coli* are $99.67 \pm 0.33\%$ and $99.70 \pm 0.29\%$ on average, respectively (Boroumand et al. 2015).

E. coli was more sensitive to silver ions than *S. aureus*, which may ascribe to the difference in the cell wall properties of two bacterial strains. For instance, the cell wall of *S. aureus* is very thick and contains a lot of surface components of mucopeptides and phosphatidic acid (Applerot et al. 2012), which can

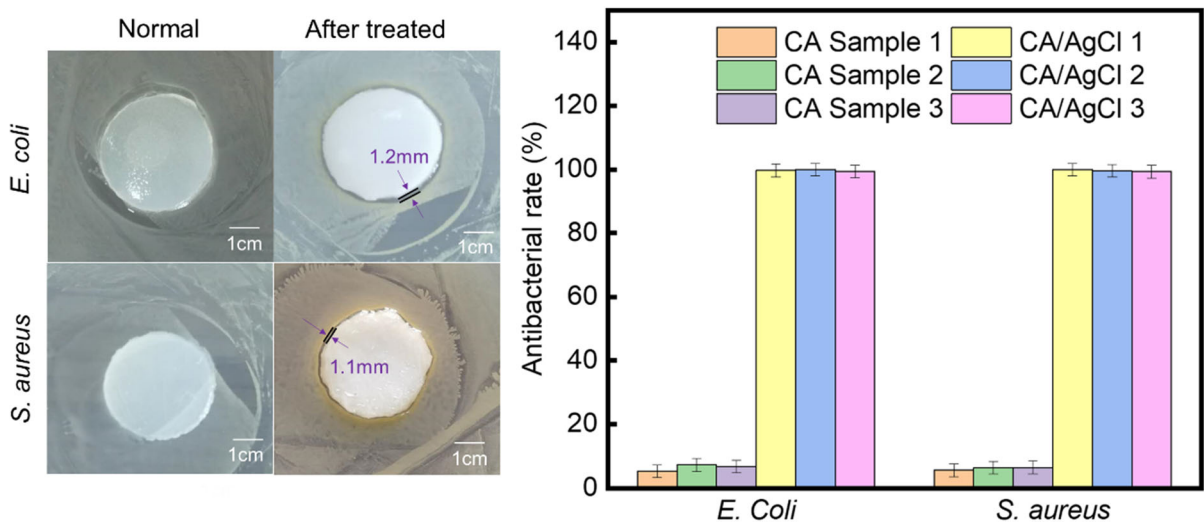


Fig. 10 Inhibition zone of CA (a) and CA/AgCl (b) hydrogel in *E. coli* medium; inhibition zone of CA (c) and CA/AgCl (d) hydrogel in *S. aureus* medium; antibacterial rate in *E. coli* and *S. aureus* (e)

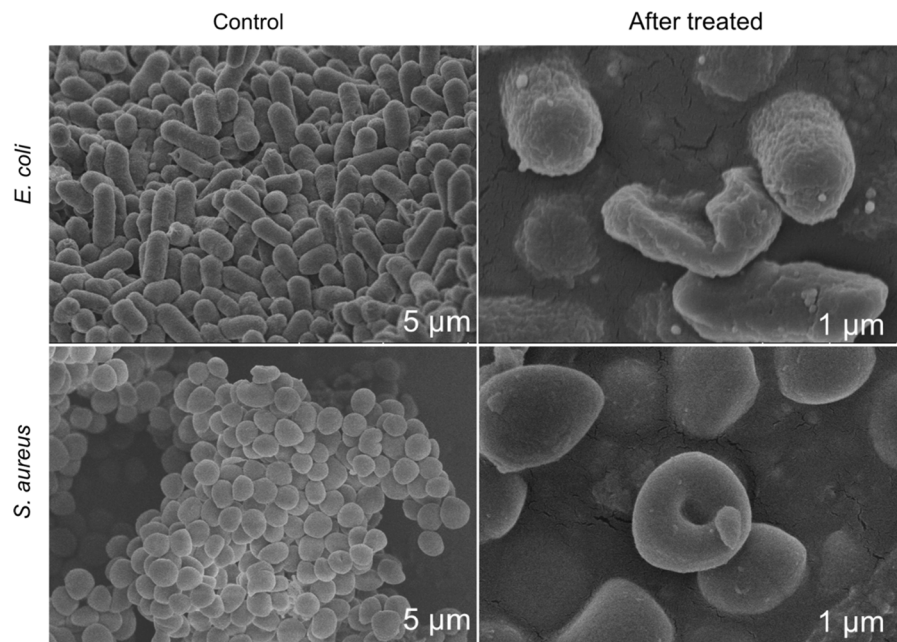


Fig. 11 SEM images for comparison of *E. coli* and *S. aureus* after treated with CA/AgCl nanocomposites

be the main reason for resulting the difference in the antibacterial rate.

Microstructure of bacteria

The morphologies of *E. coli* and *S. aureus* treated with CA/AgCl and normal status were observed by bio-

SEM, and the results are shown in Fig. 11. Intact *E. coli* cells are rod-like shape with a rough surface and *S. aureus* cells present spherical shape that was the normal morphology of bacterial growth and a necessary condition for survival. Compared with the image of normal cells, *E. coli* treated with CA/AgCl shows an abnormal wrinkled appearance, while *S. aureus*

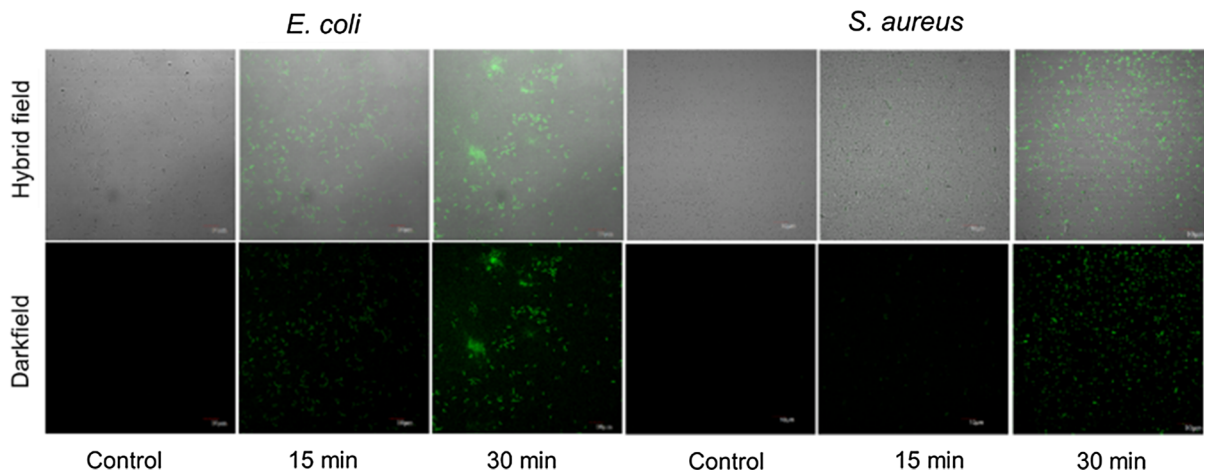


Fig. 12 Fluorescence images of *E. coli* and *S. aureus* in dark field and hybrid field treated with CA/AgCl nanocomposites for 15 and 30 min (scale bar: 10 μ m), respectively

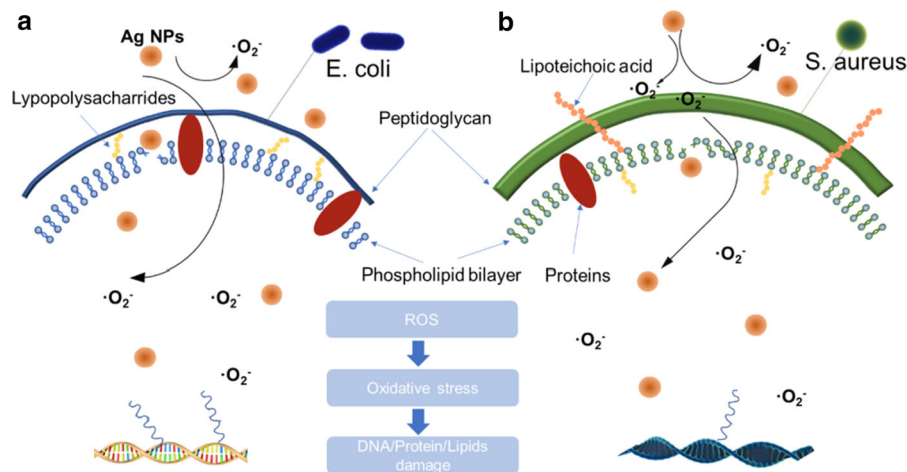


Fig. 13 Schematic illustration of antibacterial mechanism of Ag NPs and 2D structure of *E. coli* (a) and *S. aureus* (b)

bacterial membrane becomes concaved and the bacterial substrate was flowed out, reflecting the damage of bacterial cells and the cell internalization (Wu et al. 2018). The leakage of cell contents inevitably led to bacterial death. In addition, larger-sized silver particles were adsorbed on the surface of the cell membrane, which may be caused by the electrostatic interactions between the positively charged particles and the negatively charged functional protein on the cell membrane, as well as the loss of activity indirectly led to cell death. This may be the first step in the operation of the antibacterial mechanism or an auxiliary role.

The release of ROS in bacteria

DCFH-DA itself has no fluorescence and can pass through the cell membrane freely. After entering into the cell, it can be hydrolyzed by esterase in the cell to generate DCFH. However, DCFH cannot penetrate the cell membrane, so that the probe can be easily loaded into the cell. ROS in cells can oxidize non-fluorescent DCFH to produce fluorescent DCF, which can be detected to determine the level of ROS in cells.

The fluorescent probe DCFH-DA was employed to evaluate the intracellular ROS level to further explore the possible antibacterial mechanism (Panda et al. 2018). As seen in Fig. 12, normal cells show almost no

fluorescence. However, after the treatment with CA/AgCl for 15 min, the test samples exhibited weak fluorescence and most of the cells are found to maintain a complete cell structure. *S. aureus* exhibited weaker fluorescent expression than *E. coli* did in 15 min, which can be attributed to the difference of membrane. It can be also observed that after cultivating the samples for 30 min, the fluorescence in the field of view taken by the confocal microscope was significantly enhanced. However, the cell structures were destroyed. In addition, the treatment with CA/AgCl resulted in obvious increase in the fluorescence intensity. Thus, it can be concluded that the nanocomposites stimulated the release of active oxygen in the cell, and the sterilization mechanism of CA/AgCl can be attributed to the production of ROS intermediate products.

Antibacterial mechanism

Although the antibacterial effect of silver NPs have been extensively studied, a unified sterilization mechanism has not yet been formed, which is still worthy of further discussion (Rai et al. 2012).

Silver NPs can pass through the cell wall to reach to the inside of the bacteria. The oxidase-like properties of noble metals can induce the generation of reactive oxygen species (Cai et al. 2019). The generated ROS results in the internalization reaction of the cell, leading to inactivation of various enzymes, and the oxidative stress reaction causes the cell to commit suicide (Applerot et al. 2012).

Figure 13 shows the general antibacterial mechanisms and the function of silver NPs towards *E. coli* and *S. aureus*, respectively. Firstly, AgCl with a lower crystallinity enters into cells through the cell membrane (Mokhena and Luyt 2017b). Then the internalization of the cell leads to the leaching of silver ions and various enzymes react to induce oxidative stress reactions (Xu et al. 2017). Afterward, the abnormal function of various organelles causes cell leakage and death. In addition, the AgCl NPs promote the generation of oxygen anions. Especially ROS, such as superoxide anion free radicals ($\cdot\text{O}_2^-$), hydroxyl free radicals ($\cdot\text{OH}$) and hydrogen peroxide (H_2O_2) are considered to be the main products disrupting cellular homeostasis and dynamic equilibrium causing leakage of cell contents and ultimately bacterial apoptosis (Chen et al. 2019). Furthermore, the ROS can oxidize

mediated proteins, lipids and even DNA, and then lead to the loss of general functions of biofilm-related enzymes. Eventually, it causes the death of bacteria. The electrical properties of silver and Gram bacteria are opposite. After the bacteria dies, AgCl is attracted by other bacteria and continued to react with other bacteria for further repeated cycle.

Conclusions

CA/AgCl nanocomposites were synthesized via a simple and eco-friendly in-situ method. AgCl in the composites was cubic with a particle size of 20–50 nm, which was evenly distributed in the continuous phase of CA. The formed nanocomposites exhibited excellent flame-retardant property, of which the LOI exceeded 60, and the HRR and THR were significantly reduced. In particular, the amount of released smoke was notably lower than that of CA, which was only $2.7 \text{ m}^2/\text{m}^2$. It can be concluded that Ag^+ promoted the formation of char residue and bias towards to decarboxylation during the thermal degradation process. Furthermore, the nanocomposites showed remarkable antibacterial performance. The fluorescence of bacterial cells treated with CA/AgCl was significantly enhanced, which proved that the sterilization mechanism of nanocomposites was mainly related to the production of ROS intermediates. Our study proves that the nanocomposites are promising candidates for potential applications in building materials and textile industry.

Acknowledgements This work was supported by the National Natural Science Foundation of China (Grant number 51773102) and State Key Laboratory of Bio-Fibers and Eco-Textiles (Qingdao University, Grant number ZKT20). The authors wish to thank Professor Gang Wei from University of Bremen for his guidance on revising the paper and Dr. Tingting Zhang from Qingdao University for the use of some instruments and assistance with the antibacterial test.

Declaration

Conflict of interest The authors declared no conflicts of interest.

References

- Agnieszka Kyzioł JM (2017) Ivan Moreno, Enrique Gamez, Silvia Irusta Preparation and characterization of electrospun alginate nanofibers loaded with ciprofloxacin hydrochloride. *Eur Polym J* 96:350–360. <https://doi.org/10.1016/j.eurpolymj.2017.09.020>
- Applerot G, Lellouche J, Lipovsky A, Nitzan Y, Lubart R, Gedanken A, Banin E (2012) Understanding the antibacterial mechanism of CuO nanoparticles: revealing the route of induced oxidative stress. *Small* 8:3326–3337. <https://doi.org/10.1002/sml.201200772>
- Boroumand MN, Montazer M, Simon F, Liesiene J, Šaponjic Z, Dutschk V (2015) Novel method for synthesis of silver nanoparticles and their application on wool. *Appl Surf Sci* 346:477–483. <https://doi.org/10.1016/j.apsusc.2015.04.047>
- Cai T, Fang G, Tian X, Yin JJ, Chen C, Ge C (2019) Optimization of antibacterial efficacy of noble-metal-based core-shell nanostructures and effect of natural organic matter. *ACS Nano* 13:12694–12702. <https://doi.org/10.1021/acsnano.9b04366>
- Chen Y, Tang X, Gao X, Zhang B, Luo Y, Yao X (2019) Antimicrobial property and photocatalytic antibacterial mechanism of the TiO₂-doped SiO₂ hybrid materials under ultraviolet-light irradiation and visible-light irradiation *Ceram Int* 45:15505–15513. <https://doi.org/10.1016/j.ceramint.2019.05.054>
- Das D, Bang S, Zhang S, Noh I (2017) Bioactive molecules release and cellular responses of alginate-tricalcium phosphate particles hybrid gel *Nanomaterials (Basel)* 7. <https://doi.org/10.3390/nano7110389>
- De Silva RT et al (2018) Drug-loaded halloysite nanotube-reinforced electrospun alginate-based nanofibrous scaffolds with sustained antimicrobial protection. *ACS Appl Mater Inter* 10:33913–33922. <https://doi.org/10.1021/acsmi.8b11013>
- Gao L et al. (2019) Preparation, characterization and antibacterial activity of silver nanoparticle/graphene oxide/diatomite composite *Appl Surf Sci* 484:628–636. <https://doi.org/10.1016/j.apsusc.2019.04.153>
- Googerdchian F, Moheb A, Emadi R (2012) Lead sorption properties of nanohydroxyapatite–alginate composite adsorbents *Chem Eng J* 200–202:471–479. <https://doi.org/10.1016/j.cej.2012.06.084>
- Kou J, Varma RS (2012) Beet juice-induced green fabrication of plasmonic AgCl/Ag nanoparticles. *Chemoschem* 5:2435–2441. <https://doi.org/10.1002/cssc.201200477>
- Lee H et al. (2015) As(III) and As(V) removal from the aqueous phase via adsorption onto acid mine drainage sludge (AMDS) alginate beads and goethite alginate beads *J Hazard Mater* 292:146–154. <https://doi.org/10.1016/j.jhazmat.2015.03.026>
- Lee KY, Mooney DJ (2012) Alginate: properties and biomedical applications *Prog Polym Sci* 37:106–126. <https://doi.org/10.1016/j.progpolymsci.2011.06.003>
- Li D, Lv C, Liu L, Xia Y, She X, Guo S, Yang D (2015) Egg-box structure in cobalt alginate: a new approach to multifunctional hierarchical mesoporous N-doped carbon nanofibers for efficient catalysis and energy storage. *ACS Cent Sci* 1:261–269. <https://doi.org/10.1021/acscentsci.5b00191>
- Li J, Li Z, Zhao X, Deng Y, Xue Y, Li Q (2017a) Flame retardancy and thermal degradation mechanism of calcium alginate/CaCO₃ composites prepared via in situ method *J Therm Anal Calorim* 131:2167–2177. <https://doi.org/10.1007/s10973-017-6767-5>
- Li Q et al (2017) Filtration and adsorption properties of porous calcium alginate membrane for methylene blue removal from water. *Chem Eng J* 316:623–630. <https://doi.org/10.1016/j.cej.2017.01.098>
- Liu Y et al (2015) Thermal degradation and pyrolysis behavior of aluminum alginate investigated by TG-FTIR-MS and Py-GC-MS. *Polym Degrad Stab* 118:59–68. <https://doi.org/10.1016/j.polymdegradstab.2015.04.010>
- Liu Y, Wang JS, Zhu P, Zhao JC, Zhang CJ, Guo Y, Cui L (2016a) Thermal degradation properties of biobased iron alginate film. *J Anal Appl Pyrol* 119:87–96. <https://doi.org/10.1016/j.jaap.2016.03.014>
- Liu Y, Zhang CJ, Zhao JC, Guo Y, Zhu P, Wang DY (2016b) Bio-based barium alginate film: preparation, flame retardancy and thermal degradation behavior *Carbohydr Polym* 139:106–114. <https://doi.org/10.1016/j.carbpol.2015.12.044>
- Liu Y, Zhao J-C, Zhang C-J, Guo Y, Cui L, Zhu P, Wang D-Y (2015b) Bio-based nickel alginate and copper alginate films with excellent flame retardancy: preparation, flammability and thermal degradation behavior *RSC Adv* 5:64125–64137. <https://doi.org/10.1039/c5ra11048c>
- Liu Y, Zhao J-C, Zhang C-J, Guo Y, Zhu P, Wang D-Y (2015) Effect of manganese and cobalt ions on flame retardancy and thermal degradation of bio-based alginate films. *J Mater Sci* 51:1052–1065. <https://doi.org/10.1007/s10853-015-9435-9>
- Liu Y et al (2016) Effect of reactive time on flame retardancy and thermal degradation behavior of bio-based zinc alginate film. *Polym Degrad Stab* 127:20–31. <https://doi.org/10.1016/j.polymdegradstab.2015.12.024>
- Liu Z, Li J, Zhao X, Li Z, Li Q (2018a) Surface coating for flame retardancy and pyrolysis behavior of polyester fabric based on calcium alginate nanocomposites. *Nanomaterials (Basel)* 8. <https://doi.org/10.3390/nano8110875>
- Liu Z, Li Z, Zhao X, Zhang L, Li Q (2018b) Highly efficient flame retardant hybrid composites based on calcium alginate/nano-calcium borate. *Polymers (Basel)* 10 <https://doi.org/10.3390/polym10060625>
- Luo Y, Lode A, Wu C, Chang J, Gelinsky M (2015) Alginate/nanohydroxyapatite scaffolds with designed core/shell structures fabricated by 3D plotting and in situ mineralization for bone tissue engineering *ACS Appl Mater Inter* 7:6541–6549. <https://doi.org/10.1021/am508469h>
- Ma X, Li R, Zhao X, Ji Q, Xing Y, Sunarso J, Xia Y (2017) Biopolymer composite fibres composed of calcium alginate reinforced with nanocrystalline cellulose. *Compos A Appl Sci Manuf* 96:155–163. <https://doi.org/10.1016/j.compositesa.2017.02.021>
- Mokhena TC, Luyt AS (2017) Development of multifunctional nano-ultrafiltration membrane based on a chitosan thin film on alginate electrospun nanofibres. *J Clean Prod* 156:470–479. <https://doi.org/10.1016/j.jclepro.2017.04.073>

- Mokhena TC, Luyt AS (2017b) Electrospun alginate nanofibres impregnated with silver nanoparticles: preparation, morphology and antibacterial properties *Carbohydr Polym* 165:304–312. <https://doi.org/10.1016/j.carbpol.2017.02.068>
- Mu X, Yuan B, Pan Y, Feng X, Duan L, Zong R, Hu Y (2017) A single α -cobalt hydroxide/sodium alginate bilayer layer-by-layer assembly for conferring flame retardancy to flexible polyurethane foams *Mater Chem. Physics* 191:52–61. <https://doi.org/10.1016/j.matchemphys.2017.01.023>
- Nabipour H, Wang X, Song L, Hu Y (2020) Laponite-based inorganic-organic hybrid coating to reduce fire risk of flexible polyurethane foams *Appl Clay Sci* 189. <https://doi.org/10.1016/j.clay.2020.105525>
- Panda S, Rout TK, Prusty AD, Ajayan PM, Nayak S (2018) Electron transfer directed antibacterial properties of graphene oxide on metals. *Adv Mater* 30. <https://doi.org/10.1002/adma.201702149>
- Pollini M, Russo M, Licciulli A, Sannino A, Maffezzoli A (2009) Characterization of antibacterial silver coated yarns. *J Mater Sci Mater Med* 20:2361–2366. <https://doi.org/10.1007/s10856-009-3796-z>
- Rai MK, Deshmukh SD, Ingle AP, Gade AK (2012) Silver nanoparticles: the powerful nanoweapon against multidrug-resistant bacteria. *J Appl Microbiol* 112:841–852. <https://doi.org/10.1111/j.1365-2672.2012.05253.x>
- Sedighi A, Montazer M (2016) Tunable shaped N-doped CuO nanoparticles on cotton fabric through processing conditions: synthesis, antibacterial behavior and mechanical properties *Cellulose* 23:2229–2243. <https://doi.org/10.1007/s10570-016-0892-3>
- Senturk Parreidt T, Muller K, Schmid M (2018) Alginate-based edible films and coatings for food packaging applications. *Foods* 7. <https://doi.org/10.3390/foods7100170>
- Shao P, Xu P, Zhang L, Xue Y, Zhao X, Li Z, Li Q (2019) Non-chloride in situ preparation of nano-cuprous oxide and its effect on heat resistance and combustion properties of calcium alginate. *Polymers (Basel)* 11. <https://doi.org/10.3390/polym11111760>
- Wang W et al (2015) Sandwichlike coating consisting of alternating montmorillonite and β -FeOOH for reducing the fire hazard of flexible polyurethane foam. *ACS Sustain Chem Eng* 3:3214–3223. <https://doi.org/10.1021/acssuschemeng.5b00805>
- Wang Y et al. (2018) Spray-drying-assisted layer-by-layer assembly of alginate, 3-aminopropyltriethoxysilane, and magnesium hydroxide flame retardant and its catalytic graphitization in ethylene-vinyl acetate resin. *ACS Appl Mater Inter* 10:10490–10500. <https://doi.org/10.1021/acscami.8b01556>
- Wang Y, Yang X, Peng H, Wang F, Liu X, Yang Y, Hao J (2016) Layer-by-layer assembly of multifunctional flame retardant based on brucite, 3-aminopropyltriethoxysilane, and alginate and its applications in ethylene-vinyl acetate resin. *ACS Appl Mater Inter* 8:9925–9935. <https://doi.org/10.1021/acscami.6b00998>
- Wu YP, Yang Y, Zhang ZJ, Wang ZH, Zhao YB, Sun L (2018) A facile method to prepare size-tunable silver nanoparticles and its antibacterial mechanism. *Adv Powder Technol* 29:407–415. <https://doi.org/10.1016/j.apt.2017.11.028>
- Xu P, Shao P, Zhang Q, Cheng W, Li Z, Li Q (2019) A Novel Inherently Flame-Retardant Composite Based on Zinc Alginate/Nano-Cu₂O. *Polymers (Basel)* 11. <https://doi.org/10.3390/polym11101575>
- Xu ZQ et al. (2017) Tannic acid/Fe³⁺/Ag nanofilm exhibiting superior photodynamic and physical antibacterial activity. *ACS Appl Mater Inter* 9:39657–39671. <https://doi.org/10.1021/acscami.7b10818>
- Zhang C-J, Liu Y, Cui L, Yan C, Zhu P (2016) Bio-based calcium alginate nonwoven fabrics: Flame retardant and thermal degradation properties. *J Anal Appl Pyrol* 122:13–23. <https://doi.org/10.1016/j.jaap.2016.10.030>
- Zhang X, Shu Y, Su S, Zhu J (2018a) One-step coagulation to construct durable anti-fouling and antibacterial cellulose film exploiting Ag@AgCl nanoparticle- triggered photocatalytic degradation. *Carbohydr Polym* 181:499–505. <https://doi.org/10.1016/j.carbpol.2017.10.041>
- Zhang X, Xia Y, Yan X, Shi M (2018) Efficient suppression of flammability in flame retardant viscose fiber through incorporating with alginate fiber. *Mater Lett* 215:106–109. <https://doi.org/10.1016/j.matlet.2017.12.077>
- Zhao W, Qi Y, Wang Y, Xue Y, Xu P, Li Z, Li Q (2018) Morphology and thermal properties of calcium alginate/reduced graphene oxide. *Compos Polym (Basel)* 10. <https://doi.org/10.3390/polym10090990>

Publisher's Note Springer Nature remains neutral with regard to jurisdictional claims in published maps and institutional affiliations.